

Airborne lidar imaging of salmon

James H. Churnside and James J. Wilson

Lidar images of adult salmon are presented. The lidar system is built around a pulsed green laser and a gated intensified CCD camera. The camera gating is timed to collect light scattered from the turbid water below the fish to produce shadows in the images. Image processing increases the estimated contrast-to-noise ratio from 3.4 in the original image to 16.4 by means of a matched filter. © 2004 Optical Society of America

OCIS codes: 010.3640, 010.4450, 100.2980, 110.7050, 280.3640.

1. Introduction

From an aircraft it is generally difficult to see objects under the sea surface. Generally most of the light that reaches the eye is diffuse sunlight reflected from the sea surface or direct sunlight diffusely reflected from particles in the water. This is assuming that one is not looking directly onto a region of the surface where there is direct reflection of the sun and where the situation is much worse. In addition, surface waves can severely distort an image, making it more difficult to identify.

There have been several attempts to use laser illumination to reduce the effects of interference from the Sun. In one approach the laser is used in conjunction with an intensified charge coupled device (ICCD) imager that is gated so that it is on for a short time while the light of a short laser pulse is returning from some predetermined distance. This type of system has been used for both underwater^{1,2} and airborne^{3,4} imaging.

Another approach uses a streak camera to map the time of the laser pulse return onto one axis of an imaging array and the position perpendicular to the flight track onto the other axis.^{5,6} Thus each image from the array is a vertical slice through the water, and successive images along the flight track build up a full volume image, rather than a simple two-dimensional image. Another way to obtain three-

dimensional information is to scan an area with a lidar system that provides return as a function of distance. The three-dimensional approaches tend to be more expensive to implement, both in terms of the initial cost and in terms of the efficiency with which the laser energy is used.

One of the primary applications for airborne imaging of underwater objects is the detection of mines; however, attempts have also been made to use both ICCD⁷ and streak-camera⁸ imaging systems for the detection of tuna. It would appear that this same technology could be used effectively to perform aerial surveys of adult salmon as they return to their natal stream and even as they make their way upstream. This information would be very valuable to resource managers as they set harvest limits for each salmon run. Our decision to use the simpler ICCD approach, which operates in the obscuration or shadow mode, is based largely on cost and the results of various simulations.^{9–12} In this mode the laser illumination is timed so that the light is returning from below the objects of interest, which appear as shadows of the objects on the images of the light scattered from particles in the water below.

Tests were conducted on adult pink salmon (*Oncorhynchus gorbuscha*) near a hatchery on Afognak Island, Alaska. This is the smallest type of Pacific salmon, with an average adult length of 50–60 cm. It is also a commercially important species. From 1983 to 1992, an average of 77.4 million fish were caught each year in Alaska.¹³

2. Lidar System

A schematic diagram of the lidar system is presented in Fig. 1. The laser is a frequency-doubled, Q-switched Nd:YAG. It produces approximately 100 mJ of 532-nm light in a 12-ns pulse at a repetition rate of 30 Hz. The laser is polarized linearly, and

The authors are with the National Oceanic and Atmospheric Administration's Environmental Technology Laboratory, 325 Broadway, Boulder, Colorado 80305. J. H. Churnside's e-mail address is james.h.churnside@noaa.gov.

Received 2 June 2003; revised manuscript received 14 October 2003; accepted 17 October 2003.

0003-6935/04/061416-09\$15.00/0

© 2004 Optical Society of America

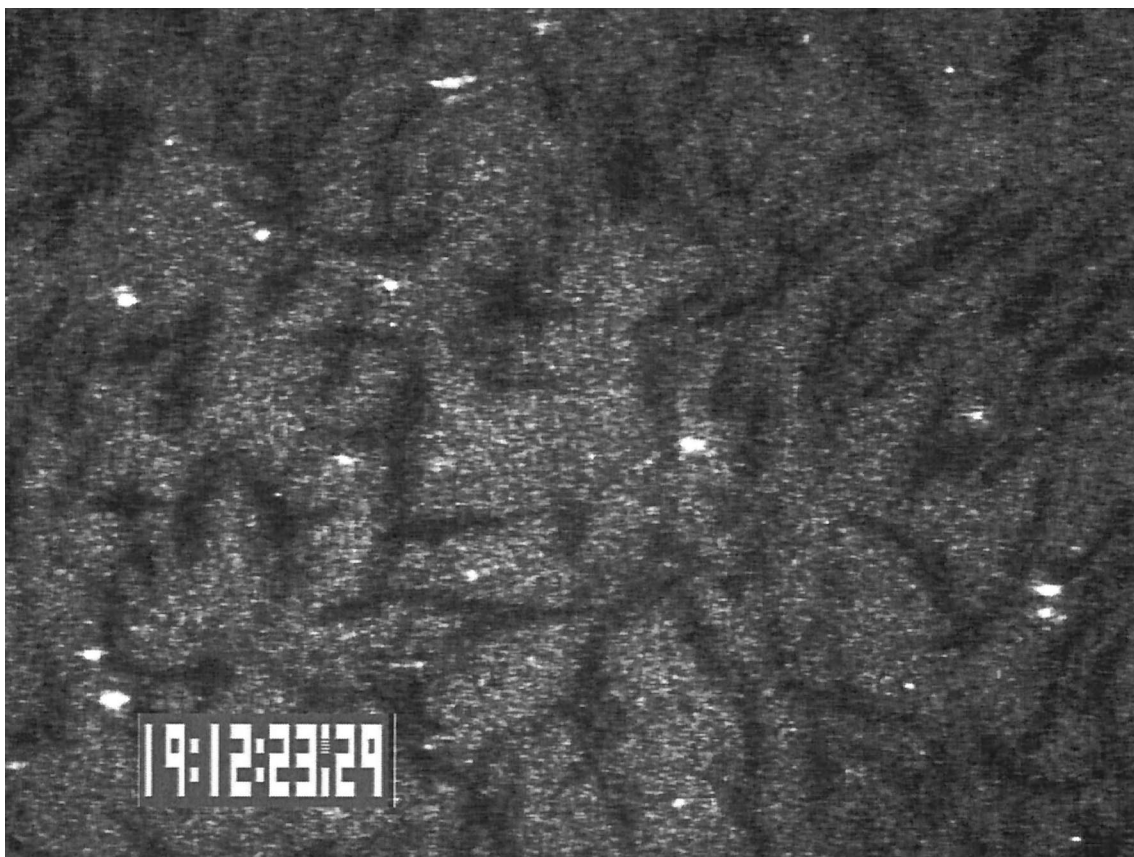


Fig. 3. Example of salmon images with surface glints.

(PMT), which converts the light signal into an electrical current. A $50\text{-}\Omega$ load resistor converts the current signal to a voltage, which is transformed with a logarithmic amplifier and digitized at 1 GHz with 8 bits of resolution (256 levels). This sample rate corresponds to a resolution of 0.11 m in depth. The

amplifier has an input voltage range from -0.2 mV to -2 V that produces an output voltage range of approximately -0.024 to -0.524 V , which implies $V_{\text{out}} = -0.125 \log(-V_{\text{in}}) - 0.486$. Because the output voltage range is well within the range of an 8-bit digitizer, the logarithmic amplifier increases the

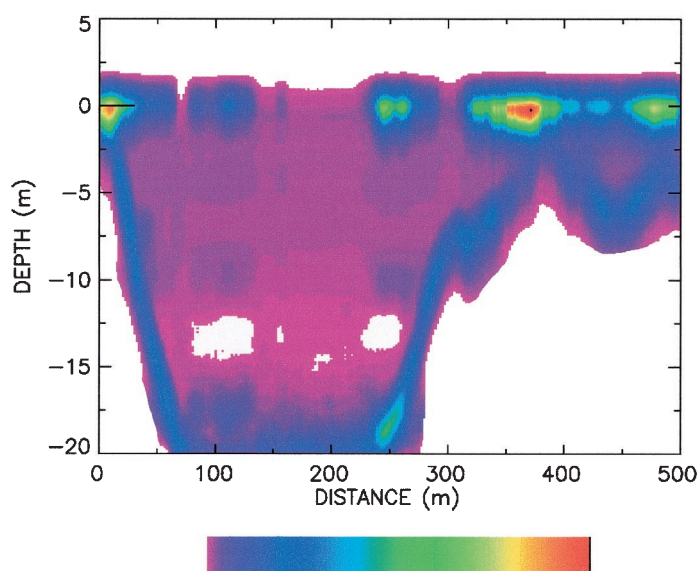


Fig. 4. Depth distribution of returns from the bay in which most of the salmon were found. The color bar represents increasing relative return from left to right. High returns near the surface are salmon, and the higher return below that is the bottom of the bay.

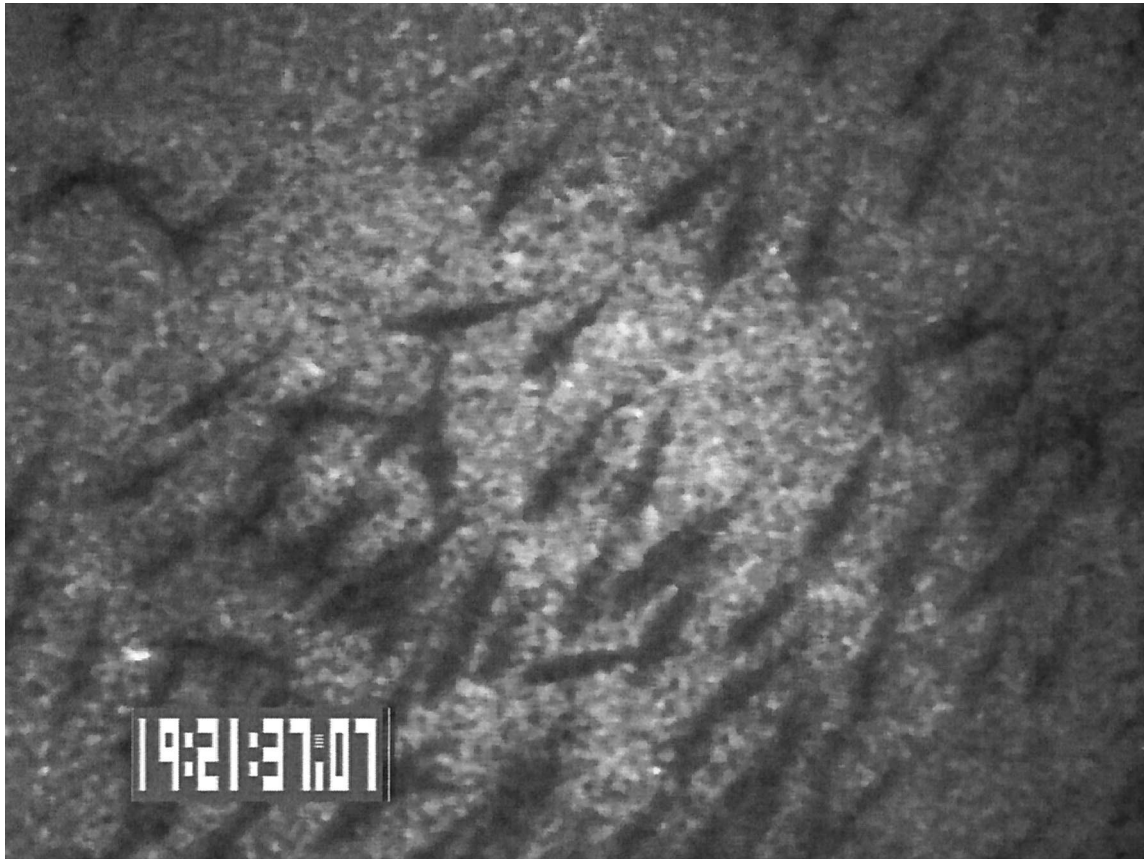


Fig. 5. Image shown in Fig. 2 after median filtering with a filter size of 5×5 pixels.

maximum possible dynamic range from 256 to $\sim 10^4$. Taken together with these components the receiver provides a depth profile of the lidar return from the fish in the water.

The signal from the profiling lidar is also used to calculate the time delay between the transmitted laser pulse and the return from the sea surface. The operator selects a desired depth of operation. The computer adds the round-trip travel time from the surface to that depth and the time delay of the surface return and programs the time-delay generator for that delay. This technique allows for imaging at a constant depth despite variations in aircraft altitude. The time delay is updated approximately eight times per second. Note that the reflection from the air–water interface preserves polarization and is not detected by our profiling receiver. The sea-surface return used for timing is actually the return from the particles just below the surface.

In addition to the log-transformed voltage signal, the computer records the aircraft position from the Global Positioning System (GPS), the GPS time, the voltage applied to the PMT, and the attitude of the aircraft as measured by tilt sensors and laser gyroscopes on the optical package. The PMT-applied voltage is used to calculate the gain of the tube, which is necessary for calibration. The computer also displays the data from the profiling lidar in real time during the flight.

The other receiver is the gated ICCD camera. The camera is equipped with a zoom lens with a focal length range of 100–500 mm. For this work it was set at 500 mm, which produced a field of view of approximately $25 \text{ mrad} \times 19 \text{ mrad}$. To reduce the amount of background light, a 10-nm-wide interference filter was mounted on the front of the lens. The intensifier is a second-generation microchannel plate with a P20 phosphor. The camera's minimum gate width of $\sim 25 \text{ ns}$ was generally used. The CCD element has a usable array of 756×485 pixels and produces an analog video signal that is recorded digitally by a mini digital video data recorder at the standard resolution of 720×480 .

The system was flown on a Beech King Air at an altitude of 150 m and at a speed of 65 ms^{-1} . Several passes were made over Kitoi Bay near the fish hatchery. The lidar settings were changed for each pass. During each pass over the bay, the aircraft was flying level, and the lidar was pointing straight down.

At the flight altitude, the image area on the surface was approximately $3.75 \text{ m} \times 2.81 \text{ m}$. The resulting pixel resolution was $0.52 \text{ cm} \times 0.59 \text{ cm}$. The digital images were resampled to 640×480 pixels to achieve the normal video aspect ratio of $4/3$ with square pixels and a resolution on the surface of $\sim 0.59 \text{ cm}$ in both dimensions. Resampling was accomplished by averaging the two or three original pixels that overlapped

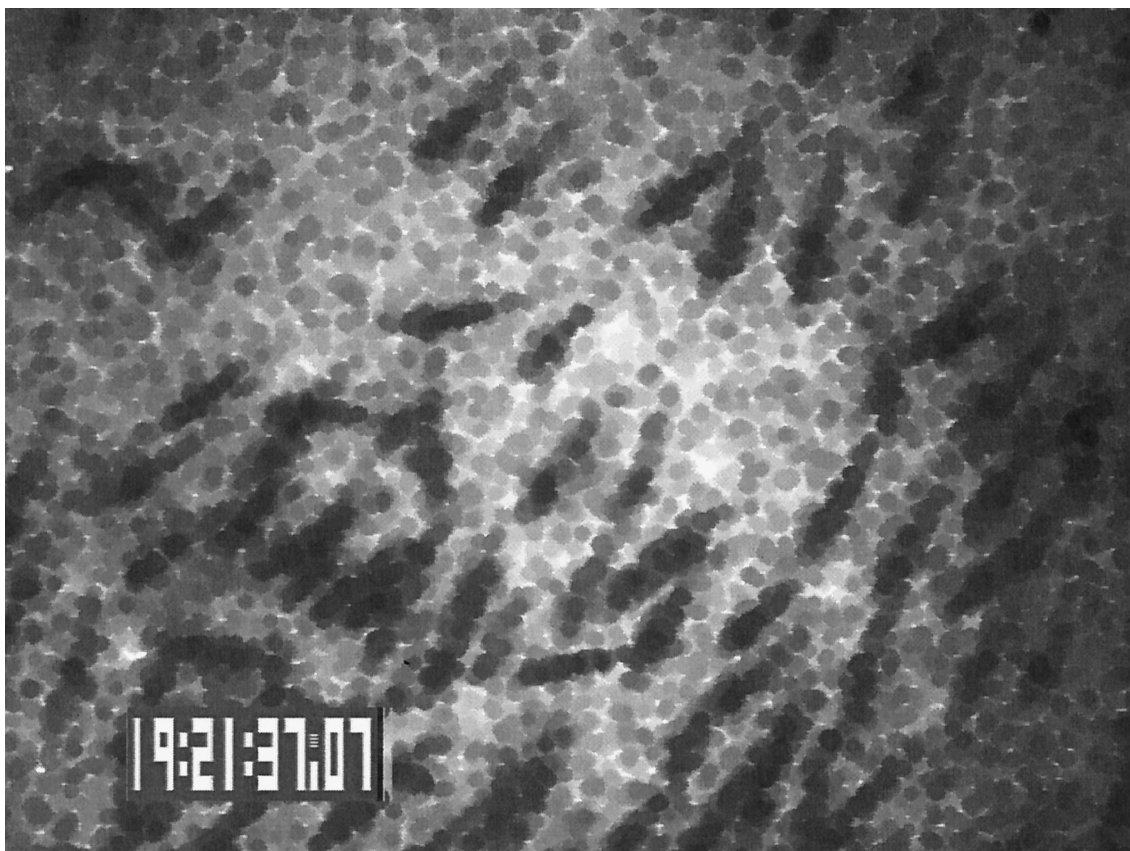


Fig. 6. Image shown in Fig. 2 after the closing operator is applied with a 9-pixel-diameter disk.

each resampled pixel, with each weighted according to the amount of overlap.

3. Results

Figure 2 shows a typical image of a group of salmon. In this case the exposure time was 20 ns. The depth of the illumination, set to a point where laser glints from the surface were not visible, is estimated to be approximately 3 m below the surface. Individual fish are easily resolved, and pectoral fins can be seen on some. Note that some of the fish, like the one labeled (a), look smaller and clearer than the others. It is likely that these fish are closer to the surface than those that appear larger and less distinct.

There are two different effects that would cause the deeper fish to appear less distinct. One is distortion caused by surface waves. The wind at the aircraft altitude was $\sim 10 \text{ m s}^{-1}$ from the west. The bay was sheltered, however, and the surface in this region appeared almost smooth with no breaking waves. From Fig. 2 we estimate the resolution of the blurrier fish to be approximately 2 cm. If we assume that these fish are no deeper than 1 m (see Fig. 4), we can estimate the root-mean-square (rms) angular distortion to be $\sim 20 \text{ mrad}$. Because the angular deviation of a vertical ray is ~ 0.75 of the surface slope, we would estimate the rms surface slope to be $\sim 27 \text{ mrad}$. This level of surface roughness can be produced by very light ($< 1 \text{ m s}^{-1}$) winds.^{18,19}

The other possible cause of the blurring is scattering of the laser light in the water. The attenuation of our beam was measured to be $\sim 0.2 \text{ m}^{-1}$, of which absorption accounts for at least 0.05 m^{-1} —and probably more.²⁰ This implies that only approximately 10%–15% of the light will be scattered between a fish at a depth of 1 m and the surface. The light that is scattered will likely have an rms angular deviation greater than 20 mrad ,²⁰ so the deeper fish would have a clear outline from the unscattered light, but reduced contrast from the scattered light. We conclude that the surface roughness effect is probably responsible for the blurring of the deeper-fish images.

Figure 3 is an example in which the depth was reduced by $\sim 1 \text{ m}$ and the exposure time was increased to 100 ns. The longer exposure time made little difference. The attenuation is so great in these waters that the exposure is almost completely determined in the first 20 ns. The shallower depth setting in places produces glints from the surface. These appear in the image as completely white regions. Note that these glints are not caused by the peak of the pulse hitting the surface but by the tail of the pulse after the peak. At this point most of the laser energy is still below the fish, which still appear as shadows. To obtain direct illumination of the salmon, we would need to use a much shorter pulse so that the depth could be decreased without causing contamination from surface glints.

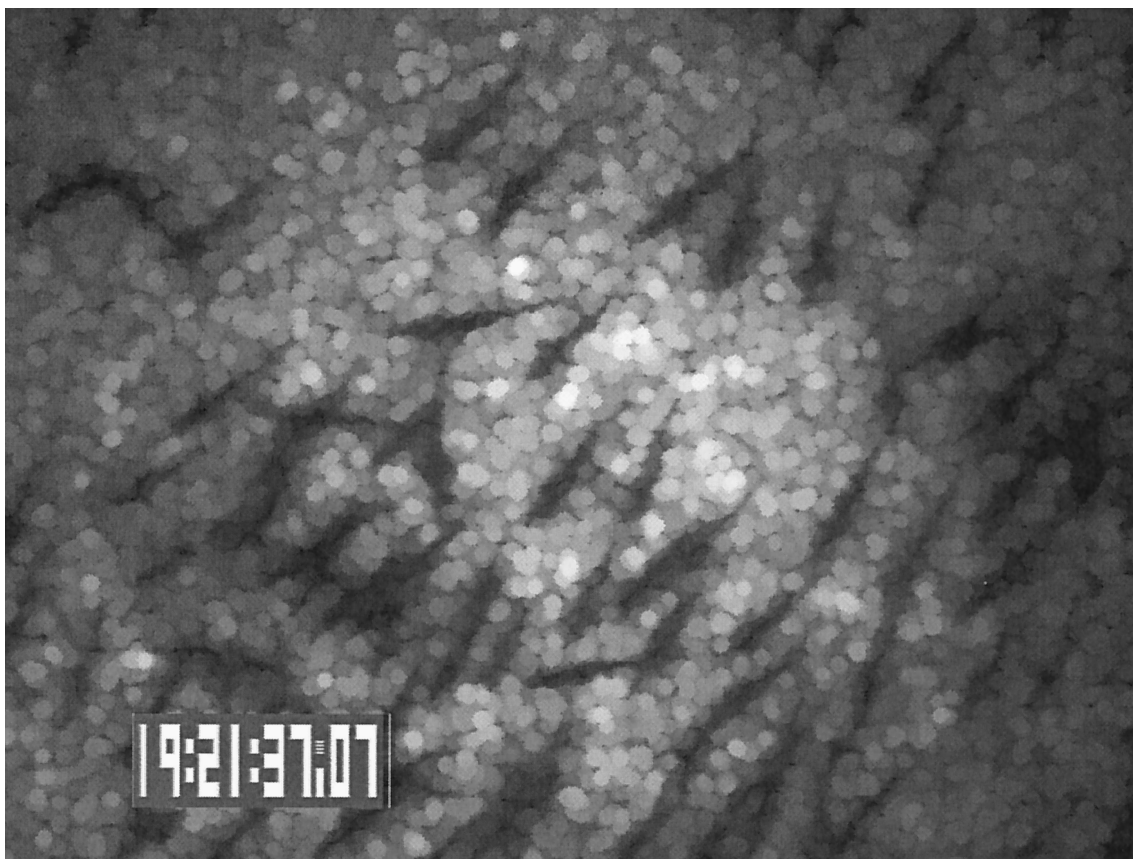


Fig. 7. Image Fig. 2 after the opening operator is applied with a 9-pixel-diameter disk.

The result of the profiling lidar from the fish shown in Fig. 2 is presented in Fig. 4, in which warm colors (yellow, orange, and red) represent higher return power. In this figure the lidar signal was corrected for depth with the average lidar attenuation coefficient measured across the bay of 0.2 m^{-1} . The fish are in schools very close to the surface. The dark-blue-to-green return below $\sim 2.5 \text{ m}$ and extending down to 20 m represents the bottom of the bay. In addition to providing a surface reference, the profiling portion of the lidar provides the thickness of the fish layer so that we can make the camera gate deep enough to capture all of the fish. This figure also demonstrates another advantage of using the cross-polarized return. If the copolarized return were used, it would be difficult to separate the specular surface reflection from the scattering from very shallow fish. The cross-polarized receiver suppresses the surface reflection so that fish can be detected all the way up to the surface.

There are a variety of image-processing techniques that can be applied to these images. There are two reasons that one might want to apply image processing. The first is to improve the appearance of the images for easier visual identification. The second is to prepare the images for automatic counting. We consider three of the most common processing techniques and examine the results of each using the image shown in Fig. 2. Fish (a) in this figure is used

as the basis for image processing. It is ~ 64 pixels long and ~ 13 pixels wide, which corresponds to a size of $38 \text{ cm} \times 8 \text{ cm}$.

One of the simplest techniques is to apply a median filter to the image to reduce the level of background noise. In this filter, each pixel is replaced by the median value of a square region of the image, centered on the pixel under consideration. The size of that filter should be such that it reduces the background noise as much as possible without overly blurring the images of the fish. Figure 5 shows the result of applying a median filter with a width of 5 pixels. The noise level has been significantly reduced, but the appearance of the fish has not changed. This type of processing would make visual identification easier. Increasing the filter size begins to blur the image and makes identification more difficult.

A slightly more complex filter applies a closing or an opening operator²¹ to the image. The closing operator is a dilation operator followed by an erosion operator. The dilation operator replaces each pixel by the local maximum over some predefined region around it, and the erosion operator replaces each pixel by the local minimum. The effect of the closing operator is to eliminate small bright features in the image without distorting the shape of larger features. In Fig. 6 we apply a closing operator by using a disk with a diameter of 9 pixels as the predefined region.

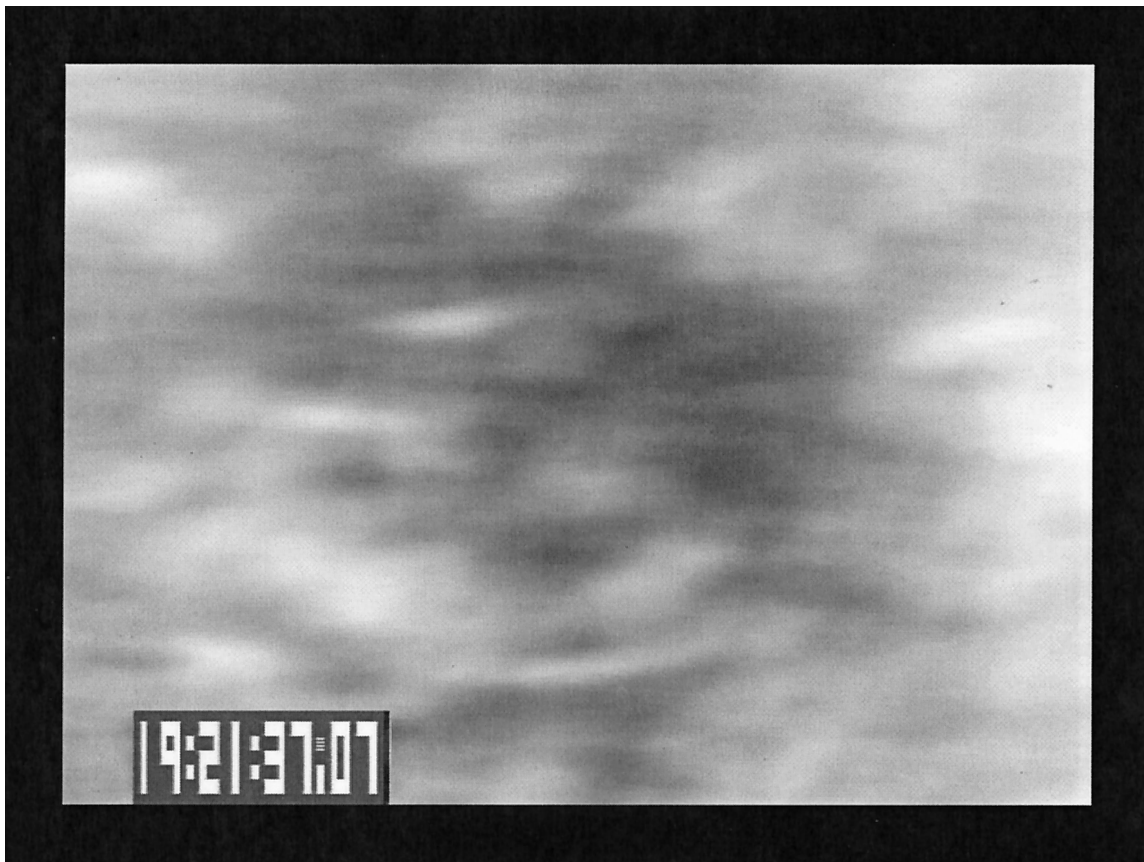


Fig. 8. Image shown in Fig. 2 after matched filtering with a horizontal ellipse.

A comparison of Figs. 5 and 6 shows that the closing operator tends to expand the outline of the fish images, making them appear larger.

The opening operator is an erosion operator followed by a dilation operator, the effect of which is to eliminate small dark features in the image. In Fig. 7, we apply an opening operator with the same predefined region. This operator tends to fill in the background around the fish, making them appear smaller. This makes the individual fish easier to identify and is probably preferable to the closing operator for this application.

A more complex filtering process can be performed by use of matched-filter processing. In this technique we calculate the convolution of the image and a filter element to create the filtered image. This convolution will have the highest values where the original image most closely matches the filter element. This technique does not produce images that are easier to identify visually. It is generally used for automatic detection of features and might be used for automatic fish counting. We based the filter on fish (a), which we model as an ellipse that is 64 pixels long and 13 pixels wide. The filter element itself is unity within this ellipse and zero outside it.

Figure 8 shows the result of the matched-filter processing when the elliptical filter is oriented horizontally. The result is a bright elliptical shape at the location of fish (a) and at several other points in the

image where there are fish that are oriented nearly horizontally. Most of the fish are oriented at $\sim 45^\circ$ from horizontal, and these appear as indistinct light areas in the processed image. In Fig. 9 we align the filter to 45° from horizontal. In this image fish (a) becomes indistinct, but most of the fish are represented by bright ellipses. Applying the same filter with different orientations produces filtered results that are largest when the fish is most closely aligned with the filter. Full matched-filter processing might use orientations spaced by 5° or 10° over the range of 0° to not quite 180° , but the results from these other orientations are not presented because most of the fish are near the 45° orientation.

To qualitatively estimate the effects of various image-processing techniques, we calculated the contrast-to-noise ratio (CNR) from two regions of the image. The first region was a 25 pixel square in the center of the fish labeled (b) in Fig. 2, and the second was a 900 pixel square in the background region just to the right of that fish. For the background region, the signal-to-noise ratio, defined as the ratio of the mean to the standard deviation of the pixel values within that region, was 4.2. The CNR was defined as

$$\text{CNR} = \frac{|\mu_F - \mu_B|}{(\sigma_F^2 + \sigma_B^2)^{1/2}}, \quad (1)$$

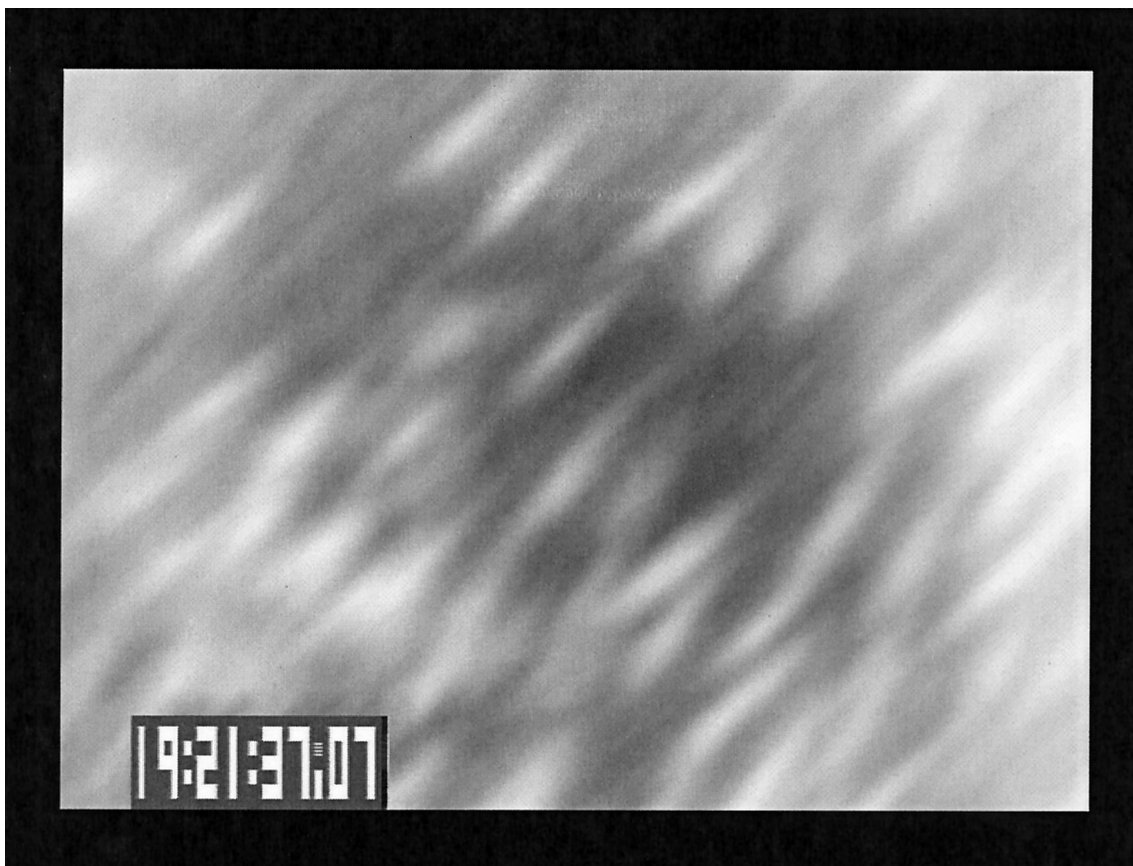


Fig. 9. Image shown in Fig. 2 after matched filtering with an ellipse rotated 45° from horizontal.

Table 1. CNR for the Fish Labeled B in Fig. 2 and the Same Fish after Various Image-Processing Operations

Image Processing	Figure Number	CNR
Original	2	3.4
Median filter	5	7.5
Opened	7	8.3
Closed	6	9.1
Matched filter (0°)	8	14.4
Matched filter (45°)	9	16.4

where μ is the mean pixel value in the region denoted by the subscript F for fish or B for background and σ^2 is the variance of pixel values in the region. The results are presented in Table 1. Image processing definitely improves the CNR by almost a factor of 5 over that calculated for the appropriate matched filter.

4. Conclusions

Individual salmon can be imaged by use of a gated ICCD camera with laser illumination. Very high resolution can be achieved, even in fairly turbid coastal waters. An important component of such a lidar system is a profiling receiver, which provides a surface reference and measures the thickness of the fish layer. A variety of standard image-processing

techniques can be used to improve the contrast of these images relative to the noise level. Some of these techniques can be used to facilitate the identification of fish in the image. It appears that discrimination among salmon and other large fish in these waters is possible based on the shape and size of the fish in the images. Discrimination among the various salmon species can be achieved in most cases by use of the size of the fish and the location and timing of the return as indicators.

Once the species is known, processing—especially matched filtering—can be used to prepare the images for possible automatic counting of fish. The development of automatic counting procedures is beyond the scope of this work. However, it is safe to say that the ultimate performance measure would not be the CNR, but the accuracy with which such a system could produce a census of the salmon in a particular region. An evaluation of this accuracy will require much more data.

This work was partially supported by the Prince William Sound Oil Spill Recovery Institute in Cordova, Alaska. The camera system was on loan from Evelyn Brown at the University of Alaska Fairbanks. Aircraft support was provided by Airborne Technologies, Incorporated of Wasilla, Alaska. The mission was flown by Phil Johnson. We were directed to the fish by Kevin Brennan of the Alaska Department of Fish and Game.

References

1. G. R. Fournier, D. Bonnier, J. L. Forand, and P. W. Pace, "Range-gated underwater imaging system," *Opt. Eng.* **32**, 2185–2190 (1993).
2. D.-M. He and G. G. L. Set, "Underwater LIDAR imaging in highly turbid waters," in *Ocean Optics: Remote Sensing and Underwater Imaging*, R. J. Frouin and G. D. Gilbert, eds., Proc. SPIE **4488**, 71–81 (2001).
3. B. L. Ulich, P. Lacovara, S. E. Moran, and M. J. DeWeert, "Recent results in imaging lidar," in *Advances in Laser Remote Sensing for Terrestrial and Oceanographic Applications*, R. M. Narayanan and J. E. Kalshoven, eds., Proc. SPIE **3059**, 95–108 (1997).
4. N. Cadalli, D. C. Munson, and A. C. Singer, "Bistatic receiver model for airborne lidar returns incident on an imaging array from underwater objects," *Appl. Opt.* **41**, 3638–3649 (2002).
5. J. W. McLean, "High-resolution 3-D underwater imaging," in *Airborne and In-Water Underwater Imaging*, G. D. Gilbert, ed., Proc. SPIE **3761**, 10–19 (1999).
6. S. T. Osofsky, "Characterization of a vertical blurring effect unique to streak tube imaging lidar," in *Ocean Optics: Remote Sensing and Underwater Imaging*, R. J. Frouin and G. D. Gilbert, eds., Proc. SPIE **4488**, 1–7 (2001).
7. C. W. Oliver and E. F. Edwards, "Dolphin-safe research program progress report II (1992–1996)," Southwest Fisheries Science Center Admin. Rep. LJ-96-13 (National Marine Fisheries Service Southwest Fisheries Science Center, La Jolla, Calif., 1996), p. 91.
8. A. J. Griffis, "Demonstration and evaluation of the streak tube imaging LIDAR for use in bycatch reduction," Saltonstall Kennedy Grant NA77FD0045 Rep. 96-SWR-010 (National Marine Fisheries Service, Southwest Region, Long Beach, Calif., 2000).
9. E. P. Zege, I. L. Katsev, A. S. Prikhach, and R. N. Keeler, "Comparison of airborne lidar performance when operating in the obscuration and reflection modes," in *Airborne and In-Water Underwater Imaging*, G. D. Gilbert, ed., Proc. SPIE **3761**, 142–153 (1999).
10. J. W. McLean and J. D. Freeman, "Effects of ocean waves on airborne lidar imaging," *Appl. Opt.* **35**, 3261–3269 (1996).
11. M. J. DeWeert, S. E. Moran, B. L. Ulich, and R. N. Keeler, "Numerical simulations of the relative performance of streak-tube, range-gated, and pmt-based airborne imaging lidar systems with realistic sea surfaces," in *Airborne and In-Water Underwater Imaging*, G. D. Gilbert, ed., Proc. SPIE **3761**, 115–129 (1999).
12. E. P. Zege, I. L. Katsev, A. S. Prikhach, and R. N. Keeler, "Simulating the performance of airborne and in-water laser imaging systems," in *Ocean Optics: Remote Sensing and Underwater Imaging*, R. J. Frouin and G. D. Gilbert, eds., Proc. SPIE **4488**, 94–105 (2001).
13. Statistics obtained from <http://www.state.ak.us/local/ak-pages/FISH.GAME/notebook/fish/pink.htm>.
14. *Safe Use of Lasers, Standard Z-136.1* (American National Standards Institute, New York, 1993).
15. H. M. Zorn, J. H. Churnside, and C. W. Oliver, "Laser safety thresholds for cetateans and pinnipeds," *Marine Mammal Sci.* **16**, 186–200 (2000).
16. J. H. Churnside, J. J. Wilson, and V. V. Tatarskii, "Lidar profiles of fish schools," *Appl. Opt.* **36**, 6011–6020 (1997).
17. J. H. Churnside, J. J. Wilson, and V. V. Tatarskii, "Airborne lidar for fisheries applications," *Opt. Eng.* **40**, 406–414 (2001).
18. C. Cox and W. Munk, "Measurements of the roughness of the sea surface from photographs of the sun's glitter," *J. Opt. Soc. Am.* **44**, 838–850 (1954).
19. J. A. Shaw and J. H. Churnside, "Scanning-laser glint measurements of sea-surface slope statistics," *Appl. Opt.* **36**, 4202–4213 (1997).
20. C. D. Mobley, *Light and Water* (Academic, San Diego, 1994).
21. R. M. Haralick, S. R. Sternberg, and X. Zhuang, "Image analysis using mathematical morphology," *IEEE Trans. Pattern Anal. Mach. Intell.* **PAMI-19**, 532–550 (1987).